Stabilization of chromatin topology safeguards genome integrity

Fena Ochs[1], Gopal Karemore[1,#], Ezequiel Miron[2,§], Jill Brown[3], Hana Sedlackova[1], Maj-Britt Rask[1], Marko Lampe[4], Veronica Buckle[3], Lothar Schermelleh[2,*], Jiri Lukas[1,*] and Claudia Lukas[1]

[1]Novo Nordisk Foundation Center for Protein Research, Faculty of Health and Medical Sciences, University of Copenhagen, Blegdamsvej 3B, 2200 Copenhagen, Denmark

[2]Micron Oxford Advanced Bioimaging Unit, Department of Biochemistry, University of Oxford, South Parks Road, Oxford OX1 3QU, United Kingdom

[3]MRC Molecular Haematology Unit, MRC Weatherall Institute of Molecular Medicine, University of Oxford, Oxford OX3 9DS, United Kingdom

[4]European Molecular Biology Laboratory, Advanced Light Microscopy Core Facility, Meyerhofstrasse 1, 69117 Heidelberg, Germany

[#]Current address, Modeling and Predictive technologies, Novo Nordisk A/S, 2760 Måløv, Denmark

[§]Current address, Division Gene regulation, The Netherlands Cancer Institute, Plesmanlaan 121, 1066 CX Amsterdam, The Netherlands

[*]Corresponding authors: jiri.lukas@cpr.ku.dk; lothar.schermelleh@bioch.ox.ac.uk

To safeguard genome integrity in response to DNA double-strand breaks (DSB), mammalian cells mobilize the neighboring chromatin to shield DNA ends against excessive resection that could undermine repair fidelity and cause damage to healthy chromosomes[1]. This form of genome surveillance is orchestrated by 53BP1, whose accumulation at DSBs triggers sequential recruitment of RIF1 and the shieldin-CST-Polα complex[2]. How this pathway reflects and impacts on the three-dimensional (3D) nuclear architecture is not known. Here, we applied super-resolution microscopy to show that 53BP1 and RIF1 form an autonomous functional module that stabilizes 3D chromatin topology at sites of DNA breakage. This is initiated by 53BP1 accrual at compact chromatin regions colocalizing with topology-associated domain (TAD) sequences and followed by RIF1 recruitment to boundaries between such domains. The alternating 53BP1 and RIF1 distribution stabilizes several neighboring TAD-sized structures at a single DBS site to an ordered, circular arrangement. Depletion of 53BP1 or RIF1 (but not shieldin) disrupts this arrangement, leading to decompaction of DSB-flanking chromatin, reduction of interchromatin space, aberrant spreading of DNA repair proteins, and DNA-end hyper-resection. Similar topological distortions are triggered by depletion of cohesin, suggesting that maintenance of chromatin structure after DNA breakage involves basic mechanisms that shape 3D nuclear organization. Since topological stabilization of DSB-flanking chromatin is independent of DNA repair, we propose that besides providing a structural scaffold to protect DNA ends against aberrant processing, 53BP1 and RIF1 safeguard epigenetic integrity at loci disrupted by DNA breakage.

To study DNA-end protection in the 3D nuclear context, we set out to visualize chromatin occupancy by 53BP1. While a typical 53BP1 repair focus appears as a homogenous sphere in conventional microscopy[3,4], 3D structured illumination microscopy (3D-SIM)[5,6] revealed an intrinsically organized compartment consisting of 4-7 53BP1-labeled sub-domains assembled in an ordered, circular fashion around a central interchromatin space (Fig. 1a). Higher resolution by stimulated emission depletion (STED) microscopy[7] refined that 53BP1 sub-domains span 60-180 nm with a center-to-center distance of approximately 140 nm (Extended Data Fig. 1a-e). We name these sub-domains 53BP1 nanodomains (53BP1-NDs) and their higher-order assembly 53BP1 microdomains (53BP1-MDs) (Extended Data Fig. 1f). Similar chromatin arrangement was detected by different SIM instruments, reproduced by independent antibodies to 53BP1, and validated by endogenous 53BP1 tagged with GFP (Extended Data Fig. 1g-k). The 53BP1 patterns mirrored phosphorylated H2AX (γH2AX) and overlapped with contained core histones (Extended Data Fig. 2a-c), in agreement with findings showing that DSB sites are organized in chromatin nanodomains[8,9]. A typical 53BP1-MD assembled around one active site of DSB repair, exemplified by a single spot of XRCC4 involved in non-homologous end joining (NHEJ) or RPA engaged in homology-directed repair (HDR) (Fig. 1b; Extended Data Fig. 2d-f). 53BP1-MDs formed in pre- and post-replicative chromatin (Fig. 1a-c), indicating a general response to DSBs.

Whereas depletion of shieldin subunits (SHLD2, SHLD3) had no impact on the 3D-arrangement of 53BP1-decorated chromatin (Fig. 1c), depletion of RIF1 disrupted 53BP1-MDs into disordered and elongated shapes characterized by misaligned 53BP-NDs (Fig. 1d). This topological disruption was quantified using a custom-designed

quantitative nanoscopy texture (QUANTEX) analysis tool, which indeed revealed a significant increase in 53BP1-MD *Mean breadth* and *Principal axis length* (Fig. 1e, f; Extended Data Fig. 3a-c). It was further reproduced by silencing RIF1 with multiple siRNAs, by replacing endogenous 53BP1 with a mutant unable to promote RIF1 recruitment[10], and in several cancer-derived as well as non-cancerous cells (Extended Data Fig. 4a-e). Together, these data indicate that 53BP1 and RIF1 form an autonomous module where RIF1 is required to stabilize 53BP1-NDs into ordered, circular chromatin architecture (Extended Data Fig. 4f). In support of this, knockdown of 53BP1 or RIF1 phenocopied each other by disrupting γH2AX-marked chromatin into disordered and elongated shapes (Extended Data Fig. 4g-i).

To study how 53BP1 and RIF1 cooperate to stabilize chromatin topology, we set out to determine RIF localization with respect to 53BP1. While conventional microscopy only generally indicates 53BP1 and RIF1 proximity at DSB-sites, 3D-SIM and STED revealed that RIF1 localized to the chromatin boundaries between neighboring 53BP1-NDs (Fig. 2a). To understand the purpose of this alternating localization, we tracked 53BP1 dynamics from pre- to post-damaged state using live-cell 3D-SIM (live-SIM; Extended Data Fig. 5a). The first 5-10 min after DSB generation were marked by loading of 53BP1 to DSB-flanking chromatin, aligned with previous findings obtained by conventional microscopy[11]. In the subsequent 5 min, the 53BP1 pattern matured into distinct 53BP1-ND arranged around a central interchromatin space (Fig. 2b; Extended Data Fig. 5b). This 53BP1 dynamics was mirrored by γH2AX and Halo-tagged histone H2B (Extended Data Fig. 6a-c), indicating that it was rooted in a chromatin template. Live-SIM analysis of RIF1-depleted cells revealed that while the initial accumulation of 53BP1 was similar to the wild-type

99 conditions, 53BP1-NDs failed to mature to circular MDs (Fig. 2c; Extended Data Fig.
100 6d), leading to asphericity of repair foci quantified as increase in *Mean breadth* of
101 chromatin marked by γH2AX (Fig. 2d). Since quantitative image-based cytometry
102 (QIBC)[12] showed no major change in the levels of γH2AX or chromatin-bound
103 53BP1, and the number of 53BP1-NDs were not altered when analyzed by STED
104 (Extended Data Fig. 7a-d), the likely cause of topological disruptions in RIF1-
105 depleted cells was an inability to stabilize long-range chromatin interactions.
106 Unexpectedly, while these data indicated that 53BP1 and RIF1 cooperate in shaping
107 chromatin architecture around DSBs, QIBC and laser microirradiation[13]
108 independently revealed a temporal shift in their recruitment. In contrast to 53BP1,
109 which was detectable immediately after DNA breakage, RIF1 became discernible
110 only 10-15 min later when 53BP1-decorated chromatin started to mature into ordered,
111 circular arrangement (Fig. 2e, f; Extended Data Fig. 7e). Although the shieldin
112 complex resembled RIF1 by localizing to 53BP1-ND neighborhoods (Extended Data
113 Fig. 7f), its disruption did not impair their spatial arrangement Fig. 1c, e). Thus, RIF1
114 recruitment to DSB sites appears to have a unique role in stabilizing chromatin
115 topology initiated by the formation of 53BP1-NDs.
116
117 To investigate how the chromatin arrangement at the DSB sites impacts on general
118 principles of 3D nuclear organization[14], we used CRISPR-Cas9 to introduce single
119 DSBs in TADs spanning coding sequences for essential mitotic regulators KIF23 and
120 KIF11, respectively (Extended Data Fig. 8a, b). We then applied RASER-FISH[15], a
121 DNA hybridization technique that complements other TAD-scale approaches[16-19] by
122 allowing simultaneous detection of labelled FISH probes with super-resolution of
123 immunolabelled proteins. While the labelled TADs showed a similar appearance

124 regardless of DNA damage (Fig. 3a, b Extended Data Fig. 8c, d), we noticed that the
125 TAD signal in the guide-RNA targeted loci appeared smaller than the surrounding
126 53BP1-MDs (Extended Data Fig. 8e, f). This was refined by 3D-SIM, which revealed
127 that the labeled *KIF23*-TAD sequence frequently overlapped with a single 53BP1-ND
128 within a given 53BP1-MD (Fig. 3a). When the sequences of 2 neighboring *KIF11*-
129 TADs (one targeted by guide-RNA and the other free of DNA damage) were labeled,
130 the RASER-FISH signals colocalized with two distinct 53BP1-NDs (Fig. 3b;
131 Extended Data Fig. 8g). Together, these data define a single 53BP1-MD as a 3D
132 multi-TAD assembly. To test whether this might be linked to mechanisms that shape
133 3D nuclear architecture[20], we knocked down cohesin subunits (RAD21, SMC1) by
134 siRNA in U2OS cells or depleted RAD21 by an auxin-inducible degron in HCT116
135 cells. In all conditions, cohesin deficiency phenocopied RIF1 knockdown by
136 disrupting 53BP1-MDs into disordered, elongated shapes without changing 53BP1 or
137 γH2AX levels (Fig. 3c, d; Extended Data Fig. 9a-j). Thus, RIF1 and cohesin
138 functionally cooperate to maintain chromatin topology at sites of DNA breakage.
139
140 Disabling NHEJ or HDR (by inhibiting DNA-PK or depleting CtIP) did not impair
141 the ordered and circular 53BP1-MD formation (Extended Data Fig. 9k-m), raising the
142 possibility that the 53BP1-initiated and RIF1-stabilized topological arrangement of
143 DSB-flanking chromatin operates as an autonomous 3D structural scaffold for repair
144 reactions. To test this, we monitored localization of BRCA1, a DNA-end processing
145 regulator that counteracts the chromatin-embedded anti-resection barrier[21]. In wild-
146 type settings, BRCA1 was confined to focal compartments either inside or at the
147 periphery of 53BP1-MDs (Fig. 3e). This dual localization likely reflects BRCA1
148 subcomplexes as only the outer, but not the inner signal could be recapitulated with

149 RAP80, a component of a BRCA1 sub-complex[22]. In RIF1-depleted cells, BRCA1
150 lost its focal appearance due to massive invasion into misshaped chromatin areas (Fig.
151 3f). This was accompanied by conversion of highly focal RPA pattern to elongated
152 structures, indicating excessive DSB resection (Fig. 3g). Whereas depletion of two
153 independent shieldin subunits also increased local BRCA1 presence at DSB sites,
154 BRCA1 remained confined to single foci and the 53BP1-MDs maintained their
155 ordered, circular shape (Fig. 3h). To investigate whether the BRCA1 mislocalization
156 in RIF1-deficient settings reflects alterations of the underlying chromatin, we
157 quantified histone H2B-GFP occupancy by 'chain analysis of the *in situ* nucleome'
158 (Cha*i*N)[23]. Intensity-based segmentation of 3D-SIM images into seven discrete H2B-
159 GFP classes (Extended Data Fig. 10a), ranging from class 1 (interchromatin space) to
160 class 7 (most compacted heterochromatin) revealed that 53BP1-MDs featured a
161 distinct distribution of chromatin classes. This distribution shifted after RIF1
162 depletion towards reduced interchromatin space (class 1) and increased chromatin
163 decompaction (classes 2 and 3) (Fig. 3i). As chromatin class distributions in
164 undamaged chromatin remained unchanged after RIF1 depletion (Extended Data Fig.
165 10b), we conclude that RIF1-mediated enforcement of compact chromatin topology is
166 confined to DSB sites.
167
168 This study reveals hitherto unknown role of 53BP1 and RIF1 in safeguarding 3D
169 structure of genomic loci disrupted by DNA breakage (Extended Data Fig. 10c). The
170 ordered topology of DSB-flanking chromatin may function as a barrier to enzymes
171 whose uncontrolled activity could cause collateral DNA and/or chromatin damage.
172 The massive spreading of BRCA1 across the topologically disordered chromatin
173 could be just the one example of structural disruptions unleashed in the absence of

53BP1 and RIF1. In addition, the compact structure of 53BP1-MDs might increase local concentration of limiting anti-resection factors such as shieldin, which are among the least abundant proteins in the human proteome (Extended Data Fig. 10d)[24,25]. Moreover, stabilized chromatin topology could provide a 3D scaffold for physiological DSBs, such as immunoglobulin diversification. The finding that 53BP1 and RIF1, but not shieldin, are required for long-range chromosomal transactions during immunoglobulin V(D)J recombination[26] are consistent with such scenario. Finally, as the topological arrangement of DSB-flanking chromatin is independent of DNA repair, and shieldins are phylogenetically younger than the upstream components of DNA-end protection pathway [24], we speculate that the 53BP1-RIF1 module might have primarily evolved to safeguard epigenetic information encrypted in 3D chromatin structure challenged by DNA breakage.

REFERENCES

1 Lukas, J., Lukas, C. & Bartek, J. More than just a focus: The chromatin response to DNA damage and its role in genome integrity maintenance. *Nat Cell Biol* **13**, 1161-1169, doi:10.1038/ncb2344 (2011).

2 Setiaputra, D. & Durocher, D. Shieldin - the protector of DNA ends. *EMBO Rep*, doi:10.15252/embr.201847560 (2019).

3 Ochs, F. *et al.* 53BP1 fosters fidelity of homology-directed DNA repair. *Nat Struct Mol Biol* **23**, 714-721, doi:10.1038/nsmb.3251 (2016).

4 Spies, J. *et al.* 53BP1 nuclear bodies enforce replication timing at under-replicated DNA to limit heritable DNA damage. *Nat Cell Biol* **21**, 487-497, doi:10.1038/s41556-019-0293-6 (2019).

198 5 Demmerle, J. *et al.* Strategic and practical guidelines for successful structured
199 illumination microscopy. *Nat Protoc* **12**, 988-1010,
200 doi:10.1038/nprot.2017.019 (2017).
201 6 Kraus, F. *et al.* Quantitative 3D structured illumination microscopy of nuclear
202 structures. *Nat Protoc* **12**, 1011-1028, doi:10.1038/nprot.2017.020 (2017).
203 7 Wegel, E. *et al.* Imaging cellular structures in super-resolution with SIM,
204 STED and Localisation Microscopy: A practical comparison. *Sci Rep* **6**,
205 27290, doi:10.1038/srep27290 (2016).
206 8 Chapman, J. R., Sossick, A. J., Boulton, S. J. & Jackson, S. P. BRCA1-
207 associated exclusion of 53BP1 from DNA damage sites underlies temporal
208 control of DNA repair. *J Cell Sci* **125**, 3529-3534, doi:10.1242/jcs.105353
209 (2012).
210 9 Natale, F. *et al.* Identification of the elementary structural units of the DNA
211 damage response. *Nat Commun* **8**, 15760, doi:10.1038/ncomms15760 (2017).
212 10 Callen, E. *et al.* 53BP1 mediates productive and mutagenic DNA repair
213 through distinct phosphoprotein interactions. *Cell* **153**, 1266-1280,
214 doi:10.1016/j.cell.2013.05.023 (2013).
215 11 Doil, C. *et al.* RNF168 binds and amplifies ubiquitin conjugates on damaged
216 chromosomes to allow accumulation of repair proteins. *Cell* **136**, 435-446,
217 doi:10.1016/j.cell.2008.12.041 (2009).
218 12 Toledo, L. I. *et al.* ATR prohibits replication catastrophe by preventing global
219 exhaustion of RPA. *Cell* **155**, 1088-1103, doi:10.1016/j.cell.2013.10.043
220 (2013).

13 Bekker-Jensen, S. *et al.* Spatial organization of the mammalian genome surveillance machinery in response to DNA strand breaks. *J Cell Biol* **173**, 195-206, doi:10.1083/jcb.200510130 (2006).

14 Marnef, A. & Legube, G. Organizing DNA repair in the nucleus: DSBs hit the road. *Curr Opin Cell Biol* **46**, 1-8, doi:10.1016/j.ceb.2016.12.003 (2017).

15 Brown, J. M. *et al.* A tissue-specific self-interacting chromatin domain forms independently of enhancer-promoter interactions. *Nat Commun* **9**, 3849, doi:10.1038/s41467-018-06248-4 (2018).

16 Bintu, B. *et al.* Super-resolution chromatin tracing reveals domains and cooperative interactions in single cells. *Science* **362**, doi:10.1126/science.aau1783 (2018).

17 Cardozo Gizzi, A. M. *et al.* Microscopy-Based Chromosome Conformation Capture Enables Simultaneous Visualization of Genome Organization and Transcription in Intact Organisms. *Mol Cell* **74**, 212-222 e215, doi:10.1016/j.molcel.2019.01.011 (2019).

18 Mateo, L. J. *et al.* Visualizing DNA folding and RNA in embryos at single-cell resolution. *Nature* **568**, 49-54, doi:10.1038/s41586-019-1035-4 (2019).

19 Nir, G. *et al.* Walking along chromosomes with super-resolution imaging, contact maps, and integrative modeling. *PLoS Genet* **14**, e1007872, doi:10.1371/journal.pgen.1007872 (2018).

20 Szabo, Q., Bantignies, F. & Cavalli, G. Principles of genome folding into topologically associating domains. *Sci Adv* **5**, eaaw1668, doi:10.1126/sciadv.aaw1668 (2019).

21 Densham, R. M. & Morris, J. R. The BRCA1 Ubiquitin ligase function sets a new trend for remodelling in DNA repair. *Nucleus* **8**, 116-125, doi:10.1080/19491034.2016.1267092 (2017).

22 Sobhian, B. *et al.* RAP80 targets BRCA1 to specific ubiquitin structures at DNA damage sites. *Science* **316**, 1198-1202, doi:10.1126/science.1139516 (2007).

23 Miron, E. *et al.* Chromatin arranges in filaments of blobs with nanoscale functional zonation. *bioRxiv*, doi:http://dx.doi.org/10.1101/566638 (2019).

24 Gupta, R. *et al.* DNA Repair Network Analysis Reveals Shieldin as a Key Regulator of NHEJ and PARP Inhibitor Sensitivity. *Cell* **173**, 972-988 e923, doi:10.1016/j.cell.2018.03.050 (2018).

25 Hein, M. Y. *et al.* A human interactome in three quantitative dimensions organized by stoichiometries and abundances. *Cell* **163**, 712-723, doi:10.1016/j.cell.2015.09.053 (2015).

26 Ghezraoui, H. *et al.* 53BP1 cooperation with the REV7-shieldin complex underpins DNA structure-specific NHEJ. *Nature* **560**, 122-127, doi:10.1038/s41586-018-0362-1 (2018).

FIGURE LEGENDS

Figure 1 | DSBs are surrounded by 53BP1 nanodomains (53BP1-NDs) arranged to higher-order 53BP1 microdomains (53BP1-MDs) in RIF1-dependent manner. **a**, 3D-SIM of GFP-53BP1-MDs in U2OS cells exposed to IR (1 Gy, 2 h). **b**, 3D-SIM of GFP-53BP1-MDs with immunostained XRCC4 (top) or RPA70 (bottom) in U2OS cells exposed to IR (1 Gy) for indicated times. **c**, **d**, 3D-SIM of immunostained 53BP1-MDs after depletion of SHLD2 (**c**, left), SHLD3 (**c**, right) and RIF1 (**d**) in

cells treated as in **a**. **e,** QUANTEX analysis of *Mean breadth* of 53BP1-MDs in cells treated as in **c**; n = 40 per condition. **f**, QUANTEX analysis of *Mean breadth* of 53BP1-MDs in cells treated as in **d**; n = 61 per condition. Box plot center lines in **e-f** are medians, boxes are 25th and 75th centiles, whiskers are min/max values, dots are outliers. *P* = 0.95, 0.51, 0.60, 0.50 (**e,** left to right) and ****P = 3.8003 x 10^{-09}, 1.6698 x 10^{-09} (**f,** left to right). NS = not significant; two-tailed non-parametric Wilcoxon rank sum test. Insets in **a**, **c**, **d** are magnified 53BP1-MDs. Cell cycle stage was determined by MCM status (MCM+ pre-replicative; MCM- post-replicative). Scale bars 5 μm in whole-nucleus images **a**, **c**, **d** and 200 nm in insets **a**, **c**, **d** and in **b**. Experiments in **a**-**f** were biologically replicated twice with similar results. For detailed image information see Supplementary Table 1.

Figure 2 | RIF1 localizes to 53BP1-NDs neighborhoods to stabilize ordered and circular architecture of 53BP1-MDs after DNA breakage.

a, Images of GFP-53BP1-MDs in U2OS cells exposed to IR (1 Gy, 2 h), immunostained for RIF1 and acquired with conventional (widefield, confocal) or super-resolution (3D-SIM, 2D-STED) microscopy. Pearson correlation coefficient (PCC = 0.25, n = 270 MDs) showing low colocalization of 53BP1 and RIF1 was derived from 3D-SIM. **b**, Live-SIM recording of an evolving GFP-53BP1-MD at a single DSB induced by neocarzinostatin (NCS, 10 ng/mL). Manual classification of main transition is color-coded. **c**, Live-SIM as in **b** in cells depleted of RIF1. **d**, QUANTEX analysis of *Mean breadth* of γH2AX-MDs in U2OS cells treated with the indicated siRNAs at the indicated times after IR (1 Gy); n = 40 per condition. Box plot center lines are medians, boxes are 25th and 75th centiles, whiskers are min/max values, dots are outliers. ****P = 8.2676 x 10^{-12}, ***P = 1.8363 x 10^{-04}, ****P =

1.9056 x 10^{-08}, NS $P = 0.7366$ (left panel, left to right), *$P = 0.0019$, 0.0059, ****$P =$ 3.4337 x 10^{-09}, NS, $P = 0.9264$ (right panel, left to right); two-tailed non-parametric Wilcoxon rank sum test. **e**, QIBC analysis of 53BP1 and RIF1 recruitment to DSBs in cells treated with IR (1 Gy) for the indicated times (n = 500 cells per condition, data points are means of population). **f**, 3D-SIM of GFP-53BP1-MDs and immunostained RIF1 in U2OS cells treated with IR (1 Gy) for the indicated times. Arrows indicate sites of RIF1 recruitment. Scale bars in **a**-**c**, **f** are 200 nm. Experiments in **a**, **d**-**f** were biologically replicated twice, and in **b**, **c** three times with similar results. For detailed image information see Supplementary Table 1.

Figure 3 | 53BP1-MDs comprise several TAD-sized chromatin domains whose ordered, circular arrangement protects integrity of DSB sites.

a, **b**, 3D-SIM of the KIF23-TAD (**a**; n = 15) the KIF11-TAD (**b**; n = 41) labeled with the dual-color FISH probes (FPs; FP-A and FP-B within one TAD; FP-C and FP-C in two TADs); pie charts depict co-localizations of the FP pairs with 53BP1-NDs. "Other" denotes infrequent arrangements. See Extended Data Fig. 8c, d for undamaged TADs. **c**, **d**, 3D-SIM of immunostained 53BP1 in HCT116-RAD21-mAID-mClover cells untreated (**c**) or treated (**d**) with auxin for 6 h. Insets are magnified 53BP1-MDs. **e**, 3D-SIM of GFP-53BP1-MDs in irradiated post-replicative U2OS cells (1 Gy, 2 h), immunostained for BRCA1 or RAP80. Localization frequency within 53BP1-MD was 28% (n = 100) for central BRCA1 (top), 54% (n = 100) for peripheral BRCA1 (middle), and 41% (n = 85) for peripheral RAP80 (bottom). **f**, 3D-SIM as in **e** after RIF1 depletion. Frequency of aberrantly spread BRCA1 was 85% (n = 84). **g**, 3D-SIM of GFP-53BP1-MDs immunostained for RPA70 and treated as in **e**. Localization frequencies were 86% (n = 92) for focal

RPA70 (top) and 66% (n = 61) or for elongated RPA70 (bottom). **h**, 3D-SIM as in **e** after SHLD2 or SHLD3 depletion. Frequency of increased but focal BRCA1 was 84% (n = 119) for SHLD2 depletion (top) and 73% (n = 82) for SHLD3 depletion (bottom). **i**, Cha*i*N analysis of 53BP1-MDs from wild-type cells or RIF1-depleted cells (n = 150 per condition). Values are medians +/- 95% confidence intervals. ***P* = 0.0019, 0.0080, 0.0015 (Class 1-3), NS, *P* = 0.1400, 0.6288, 0.2885, 0.1681 (Class 4-7); two-tailed Student *t*-test. Scale bars are 200 nm (**a,b, e-h** and insets in **c, d**), and 5 μm in whole-nucleus images (**c**, **d**). Experiments in **c**-**i** were biologically replicated twice with similar results. For detailed image information see Supplementary Table 1.

METHODS

Cell culture

Human retinal epithelial cell line hTERT-RPE1 (ATCC CRL-4000), BJ fibroblasts (ATCC CRL-2522), HeLa Kyoto cervical cancer cells, and U2OS osteosarcoma cell lines were grown in Dulbecco's modified Eagle's medium containing 10% heat-inactivated FBS and penicillin-streptomycin antibiotics. The following genetically modified cell line were used: U2OS cells stably expressing mouse 53BP1 N-terminally tagged to EGFP (GFP-53BP1)[3] (1 μg/mL puromycin), newly generated cell lines U2OS with endogenous 53BP1 C-terminally tagged with mEGFP (53BP1-GFP), U2OS cells expressing human GFP-53BP1-7A mutant (400 μg/mL geneticin), and U2OS cell line expressing GFP-53BP1/H2B-HaloTag (1 μg/mL puromycin and 400 μg/mL geneticin), U2OS-3xFLAG-SHLD3[24], HeLa H2B-GFP cells and human colorectal carcinoma HCT116 cells with integrated RAD21 degron (RAD21-mAID-mClover)[27]. HCT116 cells were cultured in McCoy's 5A modified medium with 10% FBS (100 μg/mL hygromycin and 100 μg/mL geneticin). Cells were tested for

mycoplasma on a regular basis and authenticated by STR profiling (IdentiCell Molecular Diagnostics).

Cell lines and plasmids generated for this study

U2OS GFP-53BP1-7A mutant cells were generated using plasmid pAc-GFP-human 53BP1-7A (53BP1siRNA resistant) and selection of single clones according to procedures detailed previously[3]. Plasmid was generated by cloning of a PCR fragment from FLAG-tagged 53BP1-7A (a gift from A. Shibata) into vector pAc-GFP-C1 and rendered resistant to 53BP1 siRNA (Ambion, s14313) using site-directed mutagenesis with primer CTAGAAGACCAGAAAGAGGGTCGCTCAACTAATAAGGAAAATCC. U2OS GFP-53BP1/H2B-HaloTag cells were generated by transfecting GFP-53BP1 cell line[4] with plasmid H2B-HaloTag and selection of clones[3]. Plasmid pHTC-Histone H2B-HaloTag was generated by cloning a PCR fragment of H2B from an existing H2B-GFP plasmid into Nhe1 cloning site of pHCT HaloTag CMV-neo vector (Promega, G7711) generating a C-terminal HaloTag. U2OS cells homozygously expressing C-terminally tagged 53BP1-GFP were generated using CRISPR-Cas9D10A mediated homology-directed repair[28]: cells were transfected with two pX335-U6-Chimeric_BB-CBh-hSpCas9n (D10A) plasmids (Addgene plasmid #42335)[29] expressing Cas9D10A nickase and guide RNAs (antisense: AACACAATCTCCACGATAGC, sense: GTGTAACTGGATTCCTTGCA) and donor plasmid containing mEGFP flanked by 900 bp homology arms complementary to the C-terminus of 53BP1 gene. After 7 days, GFP-positive cells were sorted by FACS (Sony SH800Z cell sorter), to obtain a heterozygous population. Homozygously-tagged 53BP1-GFP U2OS cell line was obtained by subcloning and validated by Western blot and junction PCR; forward

primer: AAGCAGCACCATTCAAGTGC and reverse primer: TCTGGGCCTTCACCTACCTT) followed by Sanger sequencing. Functionality of 53BP1-GFP was tested by DNA damage response readouts.

Generation of DNA breaks

X-ray irradiation of cells was performed using a XYLON.SMART 160E-1.5 device (160 kV, 6 mA) delivering 11.8 mGy/s. Soft X-rays were filtered by a 3 mm aluminum filter (YXLON International A/S). For laser microirradiation-induced DNA damage[13], cells were seeded on coverslips and treated with 5-bromo-2´-deoxyuridine (24 h, 10 μM Sigma B9285). The coverslip was mounted on the stage of an inverted Zeiss Axio Observer microscope equipped with a CryLaS pulsed UV-A laser (355 nm), a 40x/0.6 objective and PALM-Robo software (Version 4.5.09, Carl Zeiss MicroImaging). Laser energy output was determined by biological calibration. For temporal analysis, ten fields were irradiated for 2.5 min each along a straight-line pattern and after completion at 25 min, the coverslip was immediately fixed in 4% formaldehyde. To generate site-specific DNA breaks, cells were transfected with gRNA/Cas9 ribonucleoprotein complexes using Lipofectamine CRISPRMAX Cas9 (Invitrogen, CMAX00008). CrRNA and trcrRNA were annealed according to the manufacturer´s instructions (Integrated DNA Technologies). For transfection of a 35 mm dish (2 ml), 6.25 μL of Cas9 enzyme (TrueCut Cas9 V2, Invitrogen, A36496, 1 mg/mL) was diluted in 100 μL of Opti-MEM medium followed by addition of 12.5 μL of duplexed gRNA (2 μM) and 12.5 μL Plus-Reagent from the CRISPRMAX kit. 7.5 μL of CRISPRMAX reagent was diluted in 100 μL of Opti-MEM medium in a separate tube, mixed with the other components, incubated at RT for 15 min and added to cells. To induce DNA double-strand breaks (DSBs) for Live-SIM imaging,

cells were treated with the radiomimetic neocarzinostatin (NCS) at a final concentration of 10 ng/mL.

Gene silencing by siRNA

Transfections of siRNAs (Ambion Silencer Select) was performed with Lipofectamine RNAiMAX (Thermo Fisher Scientific, 13778075) at a concentration of 20 nM. 53BP1 (s14314, s14313), RAD21 (#1, s11726) RIF1 (#1, s30377, #2 s30378), SMC1A (#1 s15753, #2 s15751), XRCC4 (s14951). siRNA against CtIP[30] has been previously published. Ambion negative control #1 was used as control siRNA.

Other treatment of cells

DNA-PK inhibitor NU7441 (Selleckchem) was used at 10 μM, 1 h prior to IR. In order to induce RAD21 degradation in the RAD21-mAID-mClover cell line[27], cells were treated with 500 μM of the auxin component 3-indoleacetic acid, IAA (Sigma, I2886).

Antibodies for immunofluorescence (IF) detection and Western blotting

53BP1 (mouse, Millipore, MAB3802, 1:750 for IF), 53BP1 (rabbit, Novus Biologicals, NB100-305, 1:750 for IF, 1:1000 for WB), 53BP1 (rabbit, Novus Biologicals, NB100-304, 1:1000 for WB), BRCA1 (mouse, Calbiochem, O92, 1:100 for IF), CtIP (mouse, Active Motif, 61141; 1:250 for WB), FLAG-Tag (mouse, Sigma, F1804, 1:300 for IF), GFP (rabbit, Torrey Pines Biolabs, TP401, 1:1000 for WB), H2AX phospho-S139 (mouse, Abcam, ab22551, 1:1000 for IF), H2AX phospho-S139 (rabbit, Cell Signaling, 9733, 1:1000 for IF), HaloTag (mouse,

Promega, G921A, 1:1000 for WB), H2B (rabbit, Abcam, ab1790, 1:2000 for WB), KAP1 (rabbit, Bethyl Laboratories, A300-274A, 1:2000 for WB), MCM2 (mouse, Novus Biologicals, H00004171-M01, 1:200 for IF, 1:1000 for WB), MCM5 (rabbit, Abcam, ab17967, 1:200 for IF), MCM7 (mouse, Santa Cruz, sc-9966, 1:1000 for WB), MCMBP (rabbit, Novus Biologicals, NBP1-90746, 1:1000 for WB), NUDC (rabbit, Sigma-Aldrich, HPA027183, 1:1000 for WB), RAD21 (mouse, Millipore, 05-908, 1:500 for WB), RAP80 (Bethyl Laboratories, A300-764A, 1:400 for IF), RIF1 (rabbit, Bethyl Laboratories, A300-569A, 1:500 for IF), RIF1 (rabbit, Cell Signaling, 95558 , 1:500 for IF, 1:1000 for WB), RPA70 (rabbit, Abcam, ab79398, 1:300 for IF), SMC1 (rabbit, Novus Biologicals, NBP2-67733, 1:1000 for WB), tubulin (mouse, Santa Cruz, SC-8035, 1:500 for WB), XRCC4 (rabbit, Abcam, ab213729, 1: 100 for IF). MCM2 (mouse monoclonal) and MCM5 (rabbit polyclonal) antibodies were used in order to identify pre- and post-replicative cells. Secondary-antibody conjugates for immunofluorescence staining (IF) were goat anti-mouse and goat anti-rabbit Alexa Fluor 488 (A11029, A11034), Alexa Fluor 568 (A11031, A11036), Alexa Fluor 647 (A21236, A21245) reagents (Invitrogen, highly cross-adsorbed). Secondary-antibody conjugates for STED were goat anti-mouse and anti-rabbit STAR RED (Abberior, 2-0002-011-2, 2-0012-011-9) and STAR 580 goat anti-mouse and anti-rabbit (Abberior, 2-0002-005-1, 2-0012-005-8). For imaging of fixed HeLa H2B-GFP by 3D-SIM, GFP booster was used (Chromotek, gba488, 1:200). For Live-SIM, H2B-HaloTag expressing cells were labeled with 200 nM Janelia Fluor 585 HaloTag ligand (gift from Luke Lavis, HHMI Janelia) 20 min prior to image acquisition.

Western blotting

Detection of proteins by Western blotting was done using standard procedures and ECL-based chemiluminescence detection. For gel source data, see Supplementary Figure 1.

Immunofluorescence (IF) staining

Procedure for standard IF has been described previously[3]. IF for 3D-SIM was adapted from previously published protocols[5,31]. Briefly, cells were grown on square 18x18-mm or 22x22-mm #1.5H high-precision coverslips (Marienfeld Superior, thickness 0.170 +/- 0.005 mm), rinsed in PBS, pre-extracted, or not, in ice-cold 0.2% PBS-Triton-X for 1 min on ice, as indicated in Supplementary Table 1, and fixed in 4% formaldehyde for 15 min. Primary and secondary antibodies were diluted in antibody diluent (DMEM medium containing 10% FBS and 0.05% sodium azide, filtered through a 0.2 µM filter). Coverslips were washed in distilled water, mounted on a 30 µL drop of non-hardening Vectashield (Vectorlabs, H-1000) or non-hardening Slowfade Diamond (Thermo Fisher Scientific, S36963). For DAPI staining, secondary antibody solution was supplemented with 4',6'-diamidino-2-phenylindole-dyhydrochloride (DAPI, 0.5 µg/mL).

Fluorescence In-Situ-Hybridization (FISH) probes and labelling

FISH probes (FP) were generated by labeling bacterial artificial chromosome (BAC, BACPAC Resources Center, https://bacpacresources.org/) with fluorescent dyes. For detecting the TAD that harbors the KIF23 gene as annotated in the ensemble-annotated Hi-C resource at 10 kb resolution (3D Genome Browser, YUE Lab, https://promoter.bx.psu.edu/hi-c), we used two adjacent FISH-BAC probes. KIF23 FP-A is RP11-347N18, labeled with Alexa Fluor 647-aha-dUTP (A32763,

Invitrogen); KIF 23 FP-B is RP11-1150H19, labeled with Alexa Fluor 594 5-dUTP (C11400, Invitrogen), together spanning nearly the entire TAD (hg19:chr15:~ 69300000-69750000). The FISH-BAC probe FP-C for detecting the TAD that harbors the KIF11 gene (hg19:chr10:~ 94250000-94650000) was BAC probe RP742C13, labeled with Alexa Fluor 647-aha-dUTP. The FISH-BAC probe FP-D for the adjacent TAD (hg19:chr10:~ 94650000-95050000), was RP81C11, labeled with Alexa Fluor 594 5-dUTP. Comparison of these TADs in other cell lines and other data sets using the *Compare Hi-C* function of the YUE lab website, showed that they align across different cell lines and Hi-C resolution scales. BAC probes were directly labeled by nick translation as described previously[32].

Resolution After Single-strand Exonuclease Resection-FISH (RASER-FISH)

RASER-FISH maintains nuclear fine-scale structure by replacing heat denaturation with exonuclease III digestion of one of the two DNA strands after UV-generation of nicks and is suitable for super-resolution image analysis. RASER-FISH was conducted as previously described[32] and here was combined with site-specific DSB generation and IF staining of 53BP1 allowing visualization of TADs at sites of damage. As a counterpart to TADs with DSBs, undamaged TADs (Extended Data Fig. 8c, d) were selected by absence of a 53BP1 signal in the volume. Briefly, U2OS were seeded on 22x22 mm #1.5H high-precision coverslips (thickness 0.170 ± 0.005) and labeled for 24 h with 10 µM BrdU/BrdC) mix (3:1). Site-specific DSBs were induced by transfection of gRNAs for KIF23 or KIF11 (Integrated DNA Technologies, Hs.Cas9.KIF23.1.AB; Hs.Cas9.KIF11.1.AA) as described above. 3 h after gRNA transfection, cells were fixed with 4% formaldehyde (prepared from 16% formaldehyde EM grade ampules) and stained for 53BP1 as described above. After

493 incubation with DAPI for UV sensitization (0.5 µg/mL, 15 min), cells were treated
494 with UV light (254 nm, 15 min) and Exonuclease III (NEB, 5 U/µL at 37 °C, 15 min).
495 Labelled probes were denatured in hybridization mix (90 °C, 10 min) and pre-
496 annealed with human Cot-1 DNA (Invitrogen, 37 °C, 15 min) and used for
497 hybridization (39 °C, overnight). Coverslips were washed twice in 1x SSC (37 °C, 30
498 min) and once in 1x SSC at RT. Coverslips were washed in PBS, post-fixed in 4%
499 formaldehyde for10 min, rinsed in PBS and MilliQ water and mounted in Slowfade
500 Diamond.
501
502 **Microscopy and image analysis**
503 Detailed information on all images (imaging modalities, microscopy setups,
504 fluorophores, image processing, display and analysis) can be found in Supplemental
505 Table 1. Image acquisition for Quantitative Image-Based Cytometry (QIBC) by high-
506 content Widefield microscopy (ScanR Screening station, Olympus) was performed as
507 previously described[4,12]. Images were processed and analyzed using the ScanR
508 analysis software (Olympus, 2.6.1). Metrics for the different objects (number and
509 intensities of nuclei and foci) were quantified with single and calculated parameters.
510 These values were then exported and visualized with TIBCO Spotfire desktop
511 software (version 7.8.0). To visualize overlapping markers, low y-axis jittering was
512 applied in scatter plots (random displacement of objects along y-axis). Confocal
513 imaging was carried out on a LSM 880 microscope (Zeiss) or a UltraView Vox
514 spinning disk system (Perkin Elmer). Super-resolution 3D-SIM imaging was carried
515 out following previously described protocols[5], using an ELYRA PS.1 microscope
516 system (Zeiss) and a DeltaVision OMX V3 Blaze system (GE Healthcare).
517 Computational image reconstruction for ELYRA PS.1 was done using theoretical

optical transfer functions (OTFs) and the Zeiss algorithm (ZEN BLACK). For OMX V3 Blaze, raw data was reconstructed using channel-specific OTFs[5] (SoftWoRx 6.1). See Supplementary Table 1 for detailed description of imaging modalities, image processing and quality controls by SIMcheck[33]. Live cell super-resolution imaging using 3D-SIM (Live-SIM) was carried out on the DeltaVision OMX V3 Blaze system. Cells were seeded in 35 mm glass bottom dishes (thickness 170 µm ± 5 µm; Ibidi) and labeled with 200 nM Janelia Fluor 585 HaloTag ligand (gift from Luke Lavis) 20 min prior to image acquisition and washed in imaging medium (DMEM, Gibco 31053028). To induce DNA double-strand breaks (DSBs), cells were treated with NCS (10 ng/mL). Samples were imaged at 37 °C and 5% CO_2 using an Olympus 60x/1.42 NA PlanApo N objective and RI 1.520 immersion oil. 3D-SIM stacks were acquired over a 0.875 µm (7 z-planes) thick nuclear mid-section to minimize bleaching. To increase throughput, 5-10 nuclei were marked per run and 15 raw images per plane were acquired per time-point and position. The raw data was computationally reconstructed with SoftWoRx 6.1 (GE healthcare) using channel-specific OTFs as specified in Supplementary Table 1. For analysis and display, only those examples were selected that could be tracked from before to after damage, stayed in focus and did not bleach more that 30% during the whole acquisition. STED imaging was performed on an Abberior STED and RESOLFT 775 QUAD scanning microscope (Abberior Instruments GmbH) using the 488 nm CW laser and 594 nm, and 640 nm pulsed excitation lasers, and a pulsed 775 nm STED laser for depletion using a 100x/1.4 NA oil immersion objective and a 2D depletion donut for enhancing lateral resolution to approximately 50 nm. STED data was analyzed and quantified using Fiji/Image J[34].

3D-Image analysis using in-house developed QUANTEX software

QUAntitative Nanoscopy TEXture analysis (QUANTEX) is a custom image analysis software tool with a graphical user interface, developed in Matlab (R2018a, Mathworks Inc) to analyze complex 3D cellular structures. The QUANTEX software, manual and webinar can be downloaded from https://figshare.com/s/46fa39d1010d77f51d9c. QUANTEX uses 3D slice-by-slice segmentation followed by connecting segmented components in 3D. Objects are segmented via processing and segmentation algorithms, morphology filtering and advanced watershed algorithms and analyzed by original (in-house) and MathWorks algorithms for texture, geometry and morphology features. For segmentation of nuclei, z-stacks were clipped to minimum number of slices, smoothened by gaussian filter blurring, followed by automated weighted Otsu-based segmentation. 53BP1-MDs were segmented in this order: nuclear background subtraction (Rolling Ball size 3), automated Otsu segmentation, morphology filtering (minimum object size 10 voxels). Parameter output of primary and secondary object features is exported as .xlsx document. The two main QUANTEX features used in this study are *Principal axis length* and *Mean breadth*. The *Principal axis length* feature was implemented in QUANTEX from MathWorks (R2018a, MathWorks Inc.) and is a standard metric for the length of the major axis of an ellipsoid. *Mean breadth* is a metric from integral geometry and was implemented to QUANTEX from: https://github.com/mattools/matImage/blob/master/matImage/imMinkowski/imMeanBreadth. The algorithm computes the integral of mean curvature as a Minkowski measure which are estimated from the Crofton formula (see detailed information in the QUANTEX manual and webinar; https://figshare.com/s/46fa39d1010d77f51d9c.). Steps for calculating *Mean breadth* from 3D binary object: i) Calculate number of

568 voxels within the object (nv), ii) Calculate number of connected component in three
569 main direction x, y, and z (ncx, ncy, ncz), iii) Calculate number of square faces on the
570 plane with normal direction x, y and z (nfx, nfy, and nfz), iv) Calculate *Mean breadth*
571 (MB) in X direction MBx= nv - (ncy + ncz) + nfx, Y direction MBy= nv - (ncx + ncz)
572 + nfy, X direction MBz= nv - (ncx + ncy) + nfz, *Mean breadth* of an object = (MBx +
573 MBy + MBz)/3. *Principle axis length* and *Mean breadth* each measure maximum
574 linear dimension of 3D objects. Both measures consistently give significant *P* values
575 and robustly discriminate globular and elongated 53BP1-MDs. Spearman´s
576 correlation score (test association between both measures) of R sq = 0.59 (Extended
577 Data Fig. 3c) shows that they carry similar but not identical information: 59% of
578 variation in *Mean breadth* is explained by *Principle axis length* and 41% of variation
579 in *Mean breadth* is independent of the latter. Wilcoxon tests show that *Mean breadth*
580 more robustly discriminates globular and elongated shapes of 53BP1-MDs and it is
581 less susceptible to geometrical outliers; for these reasons, it was chosen as the main
582 measure in this study.
583
584 **Image analysis for Cha*i*N method (Chain analysis of the in situ-Nucleome)**
585 This image analysis pipeline was used to extract chromatin density distribution within
586 53BP1-MDs in an automated manner[23]. Reconstruced and aligned multichannel 3D-
587 SIM micrographs of chromatin and 53BP1-MDs are split into their single channel
588 components and 53BP1-MDs are thresholded by Otsu algorithm and by size exclusion
589 (excluding signal from antibody noise). The H2B chromatin channel is segmented
590 into 7 arbitrary classes implementing a Hidden Markov Model (HMM), where class 1
591 denotes no detectable chromatin (interchromatin compartment, IC), and class 2-7
592 denote increasing levels of chromatin compaction[35]. The 53BP1-MD volumes are

593 used to mask the segmented chromatin, giving the distribution of chromatin density
594 within these volumes. Aggregating these distributions over all sub-volumes for all
595 images yields an average distribution for each density class as a percentage within
596 class-specific statistical confidence ranges. As a control, the whole nuclear volume
597 can also be taken to analyse if the chromatin distribution changes genome-wide,
598 outside 53BP1-MDs. This workflow runs on free and open source software: Octave,
599 R. Scripts used can be found in the following repository:
600 https://github.com/ezemiron/Chain.
601
602 **RNA sequencing data source**
603 RNA sequencing data for 53BP1, RIF1 and SHLD1 transcripts were derived from
604 publicly available RNA sequencing data sets at EMBL-EBI expression
605 (https://www.ebi.ac.uk/gxa/home). Original data sources are: NIH Genomic Data
606 Commons Cell lines CCLE osteosarcoma (U2OS), Sanger Genomics of Drug
607 Sensitivity in Cancer Project GDSC Cancer Genome Project uterine cervix/cervical
608 carcinoma (HeLa #1), 675 Genentech uterine cervix/cervical adenocarcinoma (HeLa
609 #2), RNA seq of long poly-adenylated RNA and long non-polyadenylated RNA from
610 ENCODE cell lines/total RNA/whole cell (IMR90), Genentech RNA seq of 675
611 commonly used human cancer cell lines (HBL100, breast, normal at time of
612 derivation).
613
614 **Statistics and reproducibility**
615 Two-tailed Student t-test was used to test Gaussian distributed per-class data in Cha*i*N
616 analysis. Two-tailed non-parametric Wilcoxon rank sum test for equal medians was
617 used for all data underlying box plots except ED7d. Here, Cochran Armitage chi-

square test was applied to compare frequency distribution of an ordinal variable between different conditions. Spearman´s correlation coefficients and their R squared values were calculated for metrics *Mean breadth* and *Principal axis length* derived from control (negative class) and RIF1 depletion data (positive class) combined in order to test the association between the metrics. Pearson correlation coefficient was used to quantify the degree of colocalization between two fluorophores. Experiments were not randomized and no blinding was used during data analysis. Sample size was not pre-determined. Sample size, statistical tests and the number of biological replicates for each experiment are indicated in the figure legends.

ADDITIONAL REFERENCES

27 Rao, S. S. P. *et al.* Cohesin Loss Eliminates All Loop Domains. *Cell* **171**, 305-320 e324, doi:10.1016/j.cell.2017.09.026 (2017).

28 Koch, B. *et al.* Generation and validation of homozygous fluorescent knock-in cells using CRISPR-Cas9 genome editing. *Nat Protoc* **13**, 1465-1487, doi:10.1038/nprot.2018.042 (2018).

29 Cong, L. *et al.* Multiplex genome engineering using CRISPR/Cas systems. *Science* **339**, 819-823, doi:10.1126/science.1231143 (2013).

30 Sartori, A. A. *et al.* Human CtIP promotes DNA end resection. *Nature* **450**, 509-514, doi:10.1038/nature06337 (2007).

31 Miron, E., Innocent, C., Heyde, S. & Schermelleh, L. In Vivo and In Situ Replication Labeling Methods for Super-resolution Structured Illumination Microscopy of Chromosome Territories and Chromatin Domains. *Methods Mol Biol* **1431**, 127-140, doi:10.1007/978-1-4939-3631-1_10 (2016).

642 32 Brown, J. M. *et al.* A tissue-specific self-interacting chromatin domain forms
643 independently of enhancer-promoter interactions. *Nat Commun* **9**, 3849,
644 doi:10.1038/s41467-018-06248-4 (2018).
645 33 Ball, G. *et al.* SIMcheck: a Toolbox for Successful Super-resolution
646 Structured Illumination Microscopy. *Sci Rep* **5**, 15915, doi:10.1038/srep15915
647 (2015).
648 34 Schindelin, J. *et al.* Fiji: an open-source platform for biological-image
649 analysis. *Nat Methods* **9**, 676-682, doi:10.1038/nmeth.2019 (2012).
650 35 Smeets, D. *et al.* Three-dimensional super-resolution microscopy of the
651 inactive X chromosome territory reveals a collapse of its active nuclear
652 compartment harboring distinct Xist RNA foci. *Epigenetics Chromatin* **7**, 8,
653 doi:10.1186/1756-8935-7-8 (2014).

654

655 **DATA AVAILABILITY STATEMENT**

656 Numerical and statistical source data for Figs. 1e,f, 2d,e, 3a,b,e,f,g,h,i and Extended
657 Data Figs. 1d,e, 2c,e,f, 3b, 4d, 5c, 6c,d, 7a,b,d, 8c,d, 9c, 10b,d have been provided
658 with this manuscript. Primary imaging data underlying widefield, confocal, SIM and
659 STED images in Figs. 1a,b,c,d, 2a,b,c,f, 3a,b,c,d,e,f,g,h and Extended Data Figs.
660 1c,i,j,k, 2a,b,c, 4b,c,e,f,h,i, 5b, 6a,c,d, 7c,e,f, 8b,c,d,e,f,g, 9b,f,g,h,k,l has been
661 deposited at the European Bioinformatics Institute (EBI) BioStudies database
662 (https://www.ebi.ac.uk/biostudies/) with accession number S-BSST275. Processed
663 imaging datasets underlying QIBC, QUANTEX, Cha*i*N and other analysis, including
664 guidance on how to navigate datasets, are available from the corresponding authors.
665 There are no restrictions on data availability.

666

CODE AVAILABILITY STATEMENT

Custom Cha*i*N code is made available at https://github.com/ezemiron/Chain. Custom QUANTEX code is available from the corresponding author upon reasonable request.

ACKNOWLEDGEMENTS

The Hela Kyoto cell line was a gift from S. Narumiya. The U2OS cell line stably expressing RINN1/SHLD3 was a gift from C. Choudhary. The HCT116 cell line with endogenously integrated RAD21-mAID-mClover was a gift from E. Lieberman Aiden. The Hela cell line stably expressing Histone H2B-GFP was a gift from F. Barr. The pX335-U6-Chimeric_BB-CBh-hSpCas9n(D10A) plasmid was a gift from F. Zhang. The Flag-human53BP1-7A plasmid was a gift from A. Shibata. The JF585 dye was a gift from L. Lavis. Research funding for the Lukas lab was provided by the Novo Nordisk Foundation (grants NNF14CC0001 and NNF16CC0020906). We further acknowledge support by the Wellcome Trust Strategic Awards 091911 and 107457 supporting advanced microscopy at the Micron Oxford Advanced Bioimaging Unit (L.S.), by the Medical Research Council award MC_UU_12009/1 (J.B. and V.B.), and by the Advanced Light Microscopy Facility (ALMF) at EMBL, Heidelberg, and Abberior Instruments, Göttingen (M.L). We thank J. Dreier from the Protein Imaging Platform at Novo Nordisk Center for Protein Research for help with image analysis, and P. H. Varas from the Core Facility for Integrated Microscopy for advice on super-resolution microscopy. We thank K. Somyajit for conceptual input to this study and all members of the Lukas laboratory for useful suggestions.

AUTHOR CONTRIBUTIONS

F.O., C.L. and J.L. conceived the project. F.O. carried out all 3D-SIM, live-SIM, STED, and QIBC experiments and corresponding data analysis. G.K. performed statistical tests and developed QUANTEX together with F.O. and C.L.. H.S. performed endogenous tagging of 53BP1. L.S. developed live-SIM and supported F.O. with SIM data acquisition, data analysis and interpretation. E.M. provided Cha*i*N expertise and analyzed Cha*i*N SIM data acquired by F.O.. J.B. and V.B. provided RASER-FISH expertise and J.B. supported F.O. with sample preparation, data acquisition and analysis for RASER-FISH. M.L. taught F.O. STED imaging and supported STED data acquisition and interpretation. C.L. designed the site-specific DSB generation. M.-B.R. performed Western blots and generated cell lines. C.L., J.L. and L.S. supervised the project and together with F.O. wrote the manuscript. All authors contributed to manuscript editing.

COMPETING INTERESTS

The authors declare no competing interests.

ADDITIONAL INFORMATION

Reprints and permissions information is available online.

Supplementary information for this paper is available online.

Correspondence and request for materials should be addressed to J.L. (jiri.lukas@cpr.ku.dk) or L.S. (lothar.schermelleh@bioch.ox.ac.uk).

EXTENDED DATA LEGENDS

Extended Data Figure 1 | Spatial features of 53BP1-MDs at sites of DNA breakage.

a, Experimentally-derived resolution for STED and 3D-SIM instruments using nano-beads imaging under identical conditions as for image data acquisition at the indicated excitation wavelengths. Line profile is average of three lines, dotted line shows fit of a double Gaussian distribution, where the peak-to-peak distance indicates spatial resolution. **b**, Western blot (WB) of GFP-53BP1 U2OS cells immunostained for 53BP1, GFP and loading controls (NUDC, tubulin). **c**, 3D-SIM and STED images of immunostained 53BP1-MDs in U2OS cells exposed to IR (1Gy, 2h). Images were processed identically for pixel numbers and bicubic interpolation smoothing for direct comparison. **d**, Diameter of a 53BP1-ND in pre- and post-replicative cells determined by full width half maximum (FWHM, n = 75) from STED data in **c**. **e**, Center-to-center peak distance (n = 85) of 53BP1-NDs from STED data in **c**. Box plot center lines in **d**, **e** are medians, boxes are 25^{th} and 75^{th} centiles, whiskers are min/max values, dots are outliers. $*P = 0.0356$ **(d)**, P = 0.8587**(e)**, NS = not significant; two-tailed non-parametric Wilcoxon rank sum test. Pre- or post-replicative chromatin assigned based on MCM+/- status. **f**, Schematic depiction of 53BP1-MD. **g**, WB of U2OS cells with endogenously tagged 53BP1-GFP immunostained for 53BP1, GFP and loading control (MCM2). **h**, Junction PCR showing homozygous 53BP1 tagging. **i-k**, 3D-SIM of 53BP1 MDs in endogenously tagged U2OS-53BP1-GFP cells (**i**), U2OS cells immunostained with mouse (**j**) or rabbit (**k**) 53BP1 antibodies, exposed to IR (1 Gy, 2h). Scale bars are 100 nm (**a**) and 200 nm (**c**, **i-k**). Experiments in **b**, **d**, **e**, **g-k**) were biologically replicated twice with similar results. For detailed image information see Supplementary Table 1. For gel source data see Supplementary Figure 1.

Extended Data Figure 2 | 53BP1-MD relation to underlying chromatin.

a, 3D-SIM of GFP-53BP1-MDs in U2OS cells exposed to IR (1Gy, 2h) and immunostained for γH2AX. Pearson correlation coefficient (PCC=0.93, n = 300 MDs) shows high colocalisation of 53BP1 and γH2AX. **b**, STED of a γH2AX-MD in U2OS cells treated as in **a**. **c**, 3D-SIM of three different z-planes of HeLa cells expressing histone H2B-GFP, treated with10 ng/mL NCS for 2h, and immunostained for γH2AX. Nuclear DNA was visualized by DAPI. Insets are magnified γH2AX-MDs. Intensity line profiles of the three fluorophores (along the white line in the insets) show colocalisation of chromatin with γH2AX-MDs. **d**, WB of U2OS cells treated with control or XRCC4 siRNAs immunostained for XRCC4 and loading marker (KAP1). **e**, **f**, Intensity line profiles of 53BP1-MDs with XRCC4 (**e**) and RPA (**f**) in cells treated as in Fig. 1b; six independent examples per condition is shown. Fluorescence intensities in **c**, **e**-**f** were normalized to the maximum value of each profile. Scale bars are 200 nm in **a**, **b**, and insets (**c**) and 5 μm in whole-nucleus images (**c**). Experiments in **a**-**f** were biologically replicated twice with similar results. For detailed image information see Supplementary Table 1. For gel source data see Supplementary Figure 1.

Extended Data Figure 3 | Image analysis software QUANTEX and feature comparison for maximum linear dimension.

a, QUANTEX (QUAntitative Nanoscopy TEXture analysis) 3D image analysis workflow to analyze spatial features of 53BP1-MDs at sites of DNA damage. Step 1: 3D-SIM images are processed and segmented for cell nuclei and 53BP1-MDs using a slice-by-slice segmentation approach. Step 2: measurement for texture, morphology and geometry features are automatically derived for all segmented structures, 3D models for visual inspection are generated. Step 3: Data analysis and statistics. For

more information see Methods. **b**, QUANTEX analysis of *Principal axis length* metric of 53BP1-MDs in cells treated with control or RIF1 siRNAs. *Principal axis length* data was derived from the same experiments as in Fig. 1 a, d and represents a parallel data analysis to metric *Mean breadth* in Fig. 1f; n = 60. Box plot center lines are medians, boxes are 25th and 75th centiles, whiskers are min/max values, dots are outliers. ****P = 9.4329 x 10^{-6} (left), 2.3092 x 10^{-9} (right); two-tailed non-parametric Wilcoxon rank sum test. The experiment was biologically replicated twice with similar results. **c**, Spearman´s Correlation R squared value was calculated for *Mean breadth* and *Principal axis length* metrics derived from control (negative class, n = 90) and RIF1 depletion (positive class, n = 87) experiments combined, in order to test association. ****P = 2.74 x 10^{-35}; two-sided Spearman´s rank correlation coefficient method.

Extended Data Figure 4 | Disruption of ordered, circular arrangement of DSB-flanking chromatin after RIF1 or 53BP1 depletion.

a, WB of U2OS cells treated with control or two RIF1 siRNAs immunostained for RIF1 and loading marker (tubulin). **b,** 3D-SIM of GFP-53BP1-MDs in U2OS cells transfected with RIF1 siRNA #2 and treated as in Fig. 1d. **c**, 3D-SIM of 53BP1-MDs in U2OS cells expressing siRNA-resistant GFP-53BP1 7A mutant and depleted for endogenous 53BP1, exposed to IR (1Gy, 2h) (left). A schematic depiction of 53BP1-7A where glutamines in 7 SQ/TQ sites are converted to alanines (right). **d**, Distribution of circular with central interchromatin space (IC center) versus aspheric (no IC center) 53BP1-MDs in U2OS, HeLa Kyoto, RPE1-hTERT and BJ cells (n = 130 per condition) in control or RIF1-depleted cells treated with IR (1Gy, 2h). **e**, 3D-SIM of immunostained 53BP1-MDs in U2OS, HeLa-Kyoto, RPE1-hTERT and BJ

792 cells after control or RIF1 depletion and IR exposure (1Gy, 2h). **f**, A representative
793 3D view of an ordered, circular arrangement of GFP-53BP1-NDs in wild-type
794 conditions (top) and disordered, elongated shapes after RIF1 depletion (bottom). MIP
795 is maximal intensity projection; 3D opacity view is displayed in three orientations
796 (V1-3) indicated by colored arrows. All 3D-SIM images in this study were routinely
797 inspected this way. **g**, WB of U2OS cells treated with 53BP1 siRNA and
798 immunostained for 53BP1 and loading marker (NUDC). **h**, 3D-SIM of γH2AX-MDs
799 in U2OS cells transfected with 53BP1 siRNA and exposed to IR (1Gy, 2h). **i**, 3D-SIM
800 of GFP-53BP1 MD in U2OS cells immunostained for γH2AX and treated as in Fig.
801 1d. Insets (**b**, **c**, **h**) represent magnified single 53BP1-MDs. Scale bars are 5 μm in
802 whole-nucleus images (**b-c, h**), 200 nm in (**e, f, i**) and insets (**b, c, h**). Experiments in
803 (**a-i**) were biologically replicated twice with similar results. For detailed image
804 information see Supplementary Table 1. For gel source data see Supplementary
805 Figure 1.
806
807 **Extended Data Figure 5 | Live-SIM imaging of 53BP1-MDs; workflow and**
808 **dynamics in control cells.**
809 **a**, Schematic depiction of live 3D-SIM workflow. **b**, Live 3D-SIM of a chromosome
810 locus harboring DNA breakage under wild type conditions. U2OS-GFP-53BP1 cells
811 were treated with 10 ng/mL NCS to induce DSBs and imaged immediately for up to
812 22.5 min at 2.5 min intervals. Image galleries for seven fields from four independent
813 acquisitions are displayed. Manual classification of transition stages is color-coded.
814 Scale bars are 200 nm. For detailed image information see Supplementary Table 1.
815

816 **Extended Data Figure 6 | Live-SIM imaging of 53BP1 MDs with the underlying**
817 **chromatin and after RIF1 depletion.**
818 **a**, 3D-SIM of immunostained γH2AX-MDs in control or 53BP1-depleted U2OS cells
819 treated with IR (1Gy) of for the indicated times. **b**, WB of U2OS cells expressing
820 GFP-53BP1 and H2B-Halo-Tag immunostained for 53BP1, GFP, H2B, Halo-Tag and
821 loading marker (MCMBP). **c**, Live 3D-SIM depicting an evolving GFP-53BP1-MD at
822 a single H2B-HaloTag-labeled chromatin locus after DSB induction by NCS (10
823 ng/mL) for the indicated time-points. Insets are magnified 53BP1-MDs. Intensity line
824 profiles of the two fluorophores (along the white line in the insets) show
825 colocalisation of underlying chromatin with the 53BP1-MD. Fluorescence intensities
826 were normalized to the maximum value of each profile. **d**, Additional examples of
827 live 3D-SIM of cells treated as in Fig. 2c. Image galleries for seven fields from four
828 independent acquisitions are displayed. Manual classification of transition stages is
829 color-coded. Experiments in **a**-**c** were biologically replicated twice with similar
830 results. Scale bars in **a**, **d,** and insets in **c** are 200 nm and 1 μm in large fields in **c**. For
831 detailed image information see Supplementary Table 1. For gel source data see
832 Supplementary Figure 1.
833
834 **Extended Data Figure 7 | Analysis of RIF1 depletion, shieldin localization, and**
835 **RIF1 recruitment dynamics in the context of DSB-flanking chromatin.**
836 **a**, **b,** QIBC of fluorescence intensities associated with γH2AX MDs (**a**; n = 1000 cells
837 per condition) and 53BP1-MDs (**b**; n = 1800 cells per condition) in control or RIF1-
838 depleted cells treated with IR (1 Gy) as indicated. Box plot center lines are medians,
839 boxes are 25th and 75th centiles, whiskers are min/max values, dots are outliers. ***P
840 = 2.0631 x 10^{-10}, **P = 4.8803 x 10^{-04}, P = 0.8651, (**a**, left to right), ***P = 3.887 x

841 10^{-9}, **P** = 0.7172 (**b**, left to right), NS = not significant; two-tailed non-parametric
842 Wilcoxon rank sum test. **c**, Confocal and STED acquisitions of immunostained
843 53BP1-MDs in U2OS cells treated with control or RIF1siRNAs, exposed to IR (1Gy,
844 2h) and displayed as single and overlay images. **d**, Counts of 53BP1-NDs per 53BP1-
845 MD quantified from STED images in **c** (n = 70 per condition); horizonal bar =
846 median, *P* = 0.2711 (left), 0.9566 (right), NS = not significant; Cochran-Armitage
847 chi-square test. **e**, U2OS cells expressing endogenously tagged 53BP1-GFP were
848 treated by laser microirradiation and immunostained for γH2AX and RIF1. Asterisks
849 indicate times when γH2AX, 53BP1 and RIF1 are first detected at DSBs. **f**, 3D-SIM
850 of 53BP1-MD and 3x-FLAG-SHLD3 in U2OS cells exposed to IR (1Gy, 2h) and
851 immunostained for 53BP1 and FLAG-tag (six independent examples are shown).
852 Scale bars are 200 nm (**c**, **f**) and 20 μm (**e**). Experiments in **a**-**f** were biologically
853 replicated twice with similar results. For detailed image information see
854 Supplementary Table 1. For gel source data see Supplementary Figure 1.
855
856 **Extended Data Figure 8 | RASER-FISH analysis of 53BP1-MDs at site-specific**
857 **DSBs in *KIF23* and *KIF11* loci**
858 **a**, Depiction of a 0.45 Mb TAD from a reference cell line (adapted from Yue lab 3D
859 genome browser, see Methods) harboring the *KIF23* gene (top) and a 0.4 Mb TAD
860 harboring the *KIF11* gene (bottom). Sites of Crispr-Cas9 site-specific DSBs and a
861 position of each RASER-FISH probe (FP) are indicated. **b**, DAPI-stained U2OS cells
862 transfected with Cas9 ribonucleoprotein complexes with control, *KIF23*, or *KIF11*
863 targeting guide RNAs (gRNA). Arrows indicate examples of mitotic aberrations
864 inflicted by KIF23 and KIF11 knockout. **c**, **d**, 3D-SIM of the *KIF23*-TAD (**c**) and the
865 *KIF11*-TAD (**d**) RASER-FISH probes in cells treated as in Fig. 3a, b but at loci

without DNA damage (no 53BP1 signal). Dual-color FISH probes FP-A and FP-B in are located within the same TAD in (**c**), FP-C and FP-D in in two adjacent TADs (**d**). **e**, Widefield microscopy of immunostained 53BP1-MDs at the damaged *KIF23*-TAD locus labeled by FP-B in U2OS and RPE1-hTERT cells 3h after transfection with *KIF23* gRNA/Cas9. Insets (MD1-3) are magnified 53BP1-MDs shown in xy, xz and yz orientations. **f**, Widefield microscopy of immunostained 53BP1-MDs at the damaged *KIF11*-TAD locus labeled by FP-C in U2OS cells 3h after transfection with *KIF11* gRNA/Cas9. Insets (MD1-3) were generated as in **e**. **g**, 3D-isosurface projections (V1-3) of 3D-SIM images of FP-C and FP-D-labeled *KIF11* TADs after DNA damage induction shown in Fig. 3b. Scale bars are 5 μm in whole-nucleus images (**e**, **f**), 200 nm in insets (**e**, **f**) and in **c**, **d**, and 20 μm in **b**. Experiments in (**b**-**f**) were biologically replicated twice with similar results. For detailed image information see Supplementary Table 1.

Extended Data Figure 9 | Disruption of ordered, circular arrangement of DSB-flanking chromatin after cohesin depletion.

a, WB of HCT116-RAD21-mAID-mClover cells treated with auxin (aux) as indicated and immunostained for RAD21 and loading marker (NUDC). **b**, Widefield images of HCT116-RAD21-mAID-mClover cells, either untreated, or treated with auxin for 6h to induce RAD21 degradation. **c**, QUANTEX analysis of *Mean breadth* of 53BP1-MDs in cells treated as in Fig. 3c, d (n = 110). Box plot center lines are medians, boxes are 25th and 75th centiles, whiskers are min/max values, dots are outliers. ****P = 3.8495 x 10^{-17}, for MCM+, 7.636 x 10^{-16} for MCM-; two-tailed non-parametric Wilcoxon rank sum test. **d**, WB of U2OS cells treated with control or RAD21 siRNAs, immunostained for RAD21 and loading marker (tubulin). **e**, WB of U2OS

cells treated with control or SMC1 siRNAs, immunostained for SMC1 and loading marker (MCMBP). **f-h**, 3D-SIM of GFP-53BP1-MDs in U2OS cells transfected with RAD21 siRNA (**f**), SMC1 siRNA #1 (**g**), or SMC1 siRNA #2 (**h**) and exposed to IR (1Gy, 2h). **i**, WB of U2OS cells treated with the indicated siRNAs and immunostained for γH2AX; total protein stain is loading control. **j**, WB of U2OS cells treated with indicated siRNAs and immunostained for 53BP1 and loading marker (MCM7). **k**, **l**, 3D-SIM of GFP-53BP1-MDs in U2OS cells treated with 10 μM DNA-PK inhibitor (**k**) or CtIP siRNA (**l**), exposed to IR (1Gy, 2h). **m**, WB of U2OS cells treated with control or CtIP siRNAs, immunostained for CtIP and loading marker (NUDC). Insets in (**f-h**, **k**, **l**) are magnified 53BP1-MDs. Scale bars are 5 μm in whole-nuclei (**f-h**, **k**, **l**), 200 nm in insets (**f-h**, **k**, **l**) and 20 μm in **b**. Experiments in **a-m** were biologically replicated twice with similar results. For detailed image information see Supplementary Table 1. For gel source data see Supplementary Figure 1.

Extended Data Figure 10 | Chromatin density analysis by Cha*i*N, RNA-Seq data, and a schematic model for topological surveillance of DSB loci.

a, Schematic depiction of Cha*i*N analysis to quantify chromatin density in 3D-SIM images based on histone H2B-GFP distribution. Reconstructed and aligned 3D-SIM images were used to segment volumes occupied by 53BP1-MDs and subjected to a Hidden Markov Model (HMM) process to derive seven discrete GFP-H2B chromatin density classes within the segmented region. Class 1 represents chromatin-free interchromatin space, while class 2-7 feature increasing chromatin densities. An equivalent analysis of the whole nucleus serves as a control for global chromatin distributions outside of 53BP1-MDs. **b**, Cha*i*N analysis in undamaged nuclei in wild-

type or RIF1-depleted cells (n = 12 per condition). Values denote medians +/- 95% confidence intervals. *P = 0.0348 (Class 2), NS, P = 0.2525, 0.7373, 0.2257, 0.0990, 0.4874, 0.9496 (Class 1, 3-7); two-tailed Student t-test. **c,** A hypothetical model. A DSB triggers accumulation of 53BP1 in the damaged and several neighboring chromatin nanodomains. Saturation of 53BP1 at chromatin nanodomains prompts recruitment of RIF1 to the boundaries between them. Through functional crosstalk with cohesin, RIF1 locally stabilizes the nanodomain topology to an ordered and circular microdomain, which confines repair factors such as BRCA1 to DSBs and locally concentrates shieldin-CST-Polα to restrain DNA-end resection. Absence of RIF1 leads to topological disorder that leads to excessive spreading of BRCA1, inability to concentrate DNA-end protection factors and DSB hyper-resection. **d,** RNA sequencing data for 53BP1, RIF1 and SHLD1 transcripts per kilobase million in cancerous cells (U2OS, HeLa) and normal cells (IMR90, HBL100). Data were derived from publicly available RNA sequencing data at EMBL-EBI expression atlas (see Methods). Scale bars in **a** are 5 μm in whole-nucleus and 200 nm in the magnified 53BP1-MD (right). For detailed image information see Supplementary Table 1.

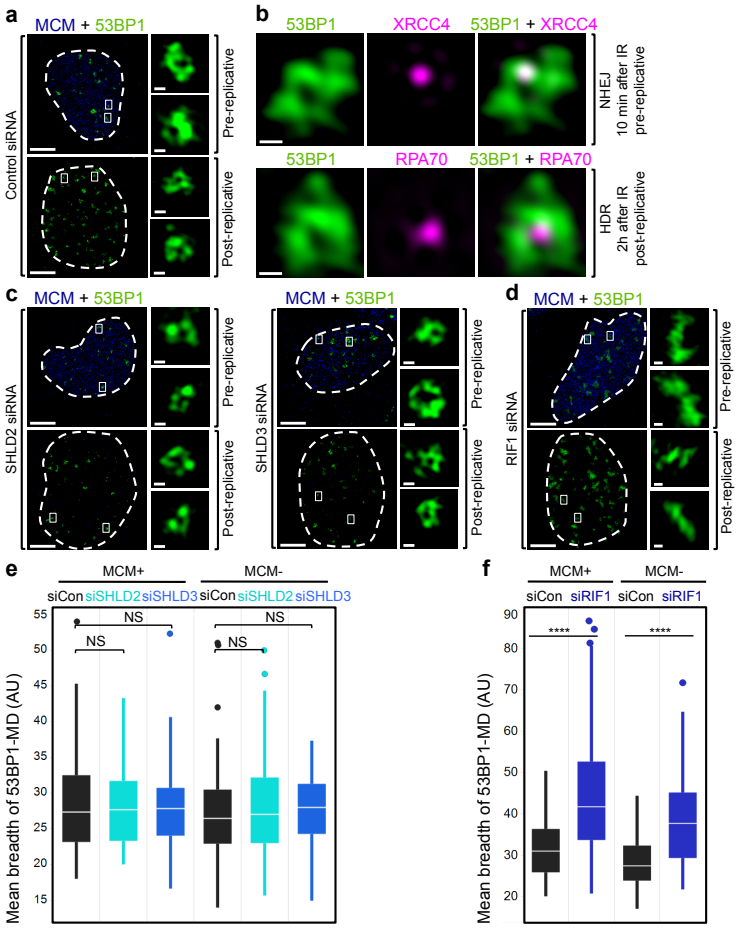
a
MCM + 53BP1
Control siRNA
Pre-replicative
Post-replicative
b
53BP1
XRCC4
53BP1 + XRCC4
NHEJ
10 min after IR
pre-replicative
53BP1
RPA70
53BP1 + RPA70
HDR
2h after IR
post-replicative
c
MCM + 53BP1
SHLD2 siRNA
SHLD3 siRNA
Pre-replicative
Post-replicative
d
MCM + 53BP1
RIF1 siRNA
Pre-replicative
Post-replicative
e
MCM+
MCM-
siCon
siSHLD2
siSHLD3
NS
Mean breadth of 53BP1-MD (AU)
f
MCM+
MCM-
siCon
siRIF1
****
Mean breadth of 53BP1-MD (AU)

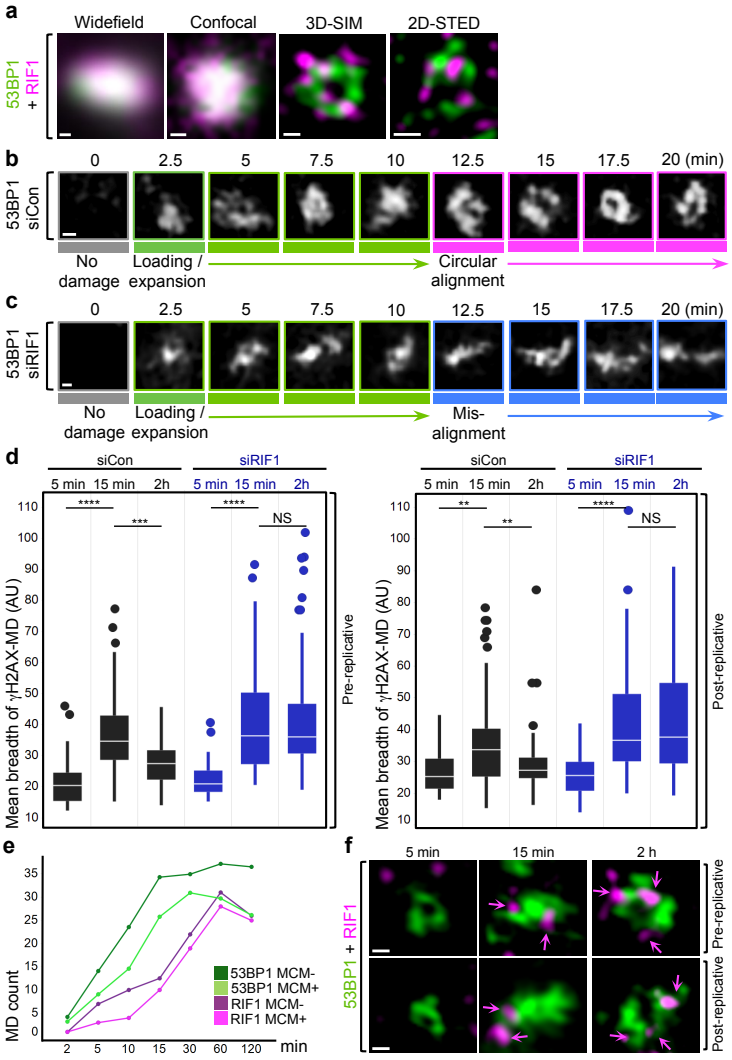
a
Widefield
Confocal
3D-SIM
2D-STED
53BP1 + RIF1
b
0
2.5
5
7.5
10
12.5
15
17.5
20 (min)
53BP1 siCon
No damage
Loading / expansion
Circular alignment
c
53BP1 siRIF1
Mis-alignment
d
siCon
siRIF1
5 min
15 min
2h
Mean breadth of γH2AX-MD (AU)
Pre-replicative
Post-replicative
****
***
NS
**
e
MD count
53BP1 MCM-
53BP1 MCM+
RIF1 MCM-
RIF1 MCM+
min
f
53BP1 + RIF1
Pre-replicative
Post-replicative

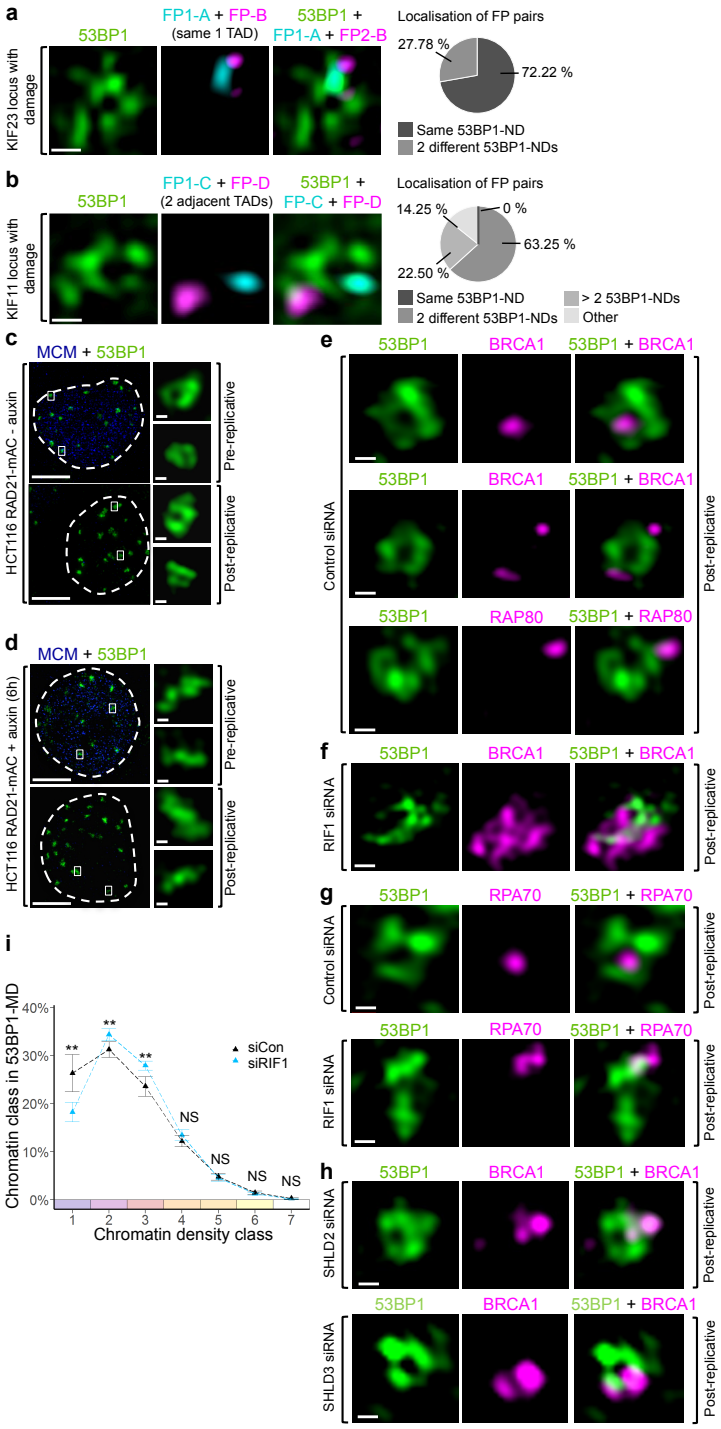
a
53BP1
FP1-A + FP-B
(same 1 TAD)
53BP1 +
FP1-A + FP2-B
KIF23 locus with damage
Localisation of FP pairs
27.78 %
72.22 %
Same 53BP1-ND
2 different 53BP1-NDs
b
53BP1
FP1-C + FP-D
(2 adjacent TADs)
53BP1 +
FP-C + FP-D
KIF11 locus with damage
Localisation of FP pairs
14.25 %
0 %
63.25 %
22.50 %
Same 53BP1-ND
2 different 53BP1-NDs
> 2 53BP1-NDs
Other
c
MCM + 53BP1
HCT116 RAD21-mAC - auxin
Pre-replicative
Post-replicative
d
MCM + 53BP1
HCT116 RAD21-mAC + auxin (6h)
Pre-replicative
Post-replicative
e
53BP1
BRCA1
53BP1 + BRCA1
Control siRNA
Post-replicative
53BP1
RAP80
53BP1 + RAP80
f
RIF1 siRNA
g
RPA70
53BP1 + RPA70
Control siRNA
RIF1 siRNA
h
SHLD2 siRNA
SHLD3 siRNA
i
Chromatin class in 53BP1-MD
40%
30%
20%
10%
0%
siCon
siRIF1
**
NS
1
2
3
4
5
6
7
Chromatin density class